Elsevier Editorial System(tm) for Journal of Natural Gas Science & Engineering
Manuscript Draft

Manuscript Number: JNGSE-D-20-00053R1

Title: Scale-span pore structure heterogeneity of high volatile bituminous coal and anthracite by FIB-SEM and X-ray μ-CT

Article Type: Full Length Article

Keywords: coals; scale-span pore structure; FIB-SEM tomography; X-ray μ-CT; 3D fractal dimension

Corresponding Author: Dr. Yidong Cai, Ph.D

Corresponding Author's Institution: China University of Geosciences, Beijing

First Author: Qian Li

Order of Authors: Qian Li; Dameng Liu; Yidong Cai, Ph.D; Bo Zhao; Yongkai Qiu; Yingfang Zhou

Abstract: Visualizing and quantifying the pore structure at the nano-micro scale is critical for understanding the micro fluid transport and enrichment in coalbed methane (CBM) reservoirs. In this work, the detailed micro-nano scale pore parameters such as pore counts, pore area, pore volume and pore size distribution can be acquired by the focused ion beam-scanning electron microscopy (FIB-SEM) and X-ray computed micro-tomography (X-ray μ-CT) techniques. Meanwhile, the pore network model (PNM) was adopted to describe and quantify the pore throat characteristics, which found that the pore throats of the sample LHG well developed and are conducive to seepage. Additionally, the three-dimensional fractal dimension (D3) by the box-counting method was used to evaluate the pores spatial heterogeneity. The D3 of sample LHG and sample L-1 are 2.23 and 2.04 (for FIB-SEM with pore size of 10 nm to ~1000 nm), 2.69 and 2.51 (for X-ray μCT with pore size over 500 nm), respectively. The results indicate that the pore network has self-similarity with a secondary development. The variable trends from tens of nanometers to micrometers through the FIB-SEM and X-ray μCT images. For the relationship between porosity and D3, two opposite trends have emerged. The positive correlation trend should be related to the complex pore structure. The more complex the pore structure is, the higher the porosity is. The negative correlation should contribute to a lot of mineral-filled pores. Pores filled with minerals that will increase the proportion of small pores and decrease the porosity, which causes that the spatial complexity of the pore networks is increased, and the D3 is increased. Therefore, this work may provide insights into the gas storage and seepage capabilities of coalbed methane (CBM) reservoirs, and thus will be favorable for enhancing CBM recovery.

Research Data Related to this Submission

There are no linked research data sets for this submission. The following reason is given:
Data will be made available on request

Highlights

- 3D pore networks of coals were compared by FIB-SEM and X-ray μCT.
- Multiscale heterogeneity of pore networks was evaluated by fractal method.
- Factors affecting the pore network complexity were revealed.

Scale-span pore structure heterogeneity of high volatile bituminous coal and anthracite by FIB-SEM and X-ray μ-CT

Qian Li[a, b], Dameng Liu[a, b], Yidong Cai [a,b]*, Bo Zhao[c], Yongkai Qiu [a, b], Yingfang Zhou[d]

[a]*School of Energy Resources, China University of Geosciences, Beijing 100083, China*

[b]*Coal Reservoir Laboratory of National Engineering Research Center of CBM Development & Utilization, China University of Geosciences, Beijing 100083, China*

[c]*School of Water Resources and Environment, China University of Geosciences, Beijing 100083, China*

[d]*School of Engineering, Fraser Noble Building, King's College, University of Aberdeen, AB24 3UE Aberdeen, UK*

Abstract

Visualizing and quantifying the pore structure at the nano-micro scale is critical for understanding the micro fluid transport and enrichment in coalbed methane (CBM) reservoirs. In this work, the detailed micro-nano scale pore parameters such as pore counts, pore area, pore volume and pore size distribution can be acquired by the focused ion beam-scanning electron microscopy (FIB-SEM) and X-ray computed micro-tomography (X-ray μ-CT) techniques. Meanwhile, the pore network model (PNM) was adopted to describe and quantify the pore throat characteristics, which found that the pore throats of the sample LHG well developed and are conducive to seepage. Additionally, the three-dimensional fractal dimension (D_3) by the box-counting method was used to evaluate the pores spatial heterogeneity. The D_3 of sample LHG and sample L-1 are 2.23 and 2.04 (for FIB-SEM with pore size of 10 nm to ~1000 nm), 2.69 and 2.51 (for X-ray μCT with pore size over 500 nm), respectively. The results indicate that the pore network has self-similarity with

a secondary development. The variable trends from tens of nanometers to micrometers through the FIB-SEM and X-ray μCT images. For the relationship between porosity and D_3, two opposite trends have emerged. The positive correlation trend should be related to the complex pore structure. The more complex the pore structure is, the higher the porosity is. The negative correlation should contribute to a lot of mineral-filled pores. Pores filled with minerals that will increase the proportion of small pores and decrease the porosity, which causes that the spatial complexity of the pore networks is increased, and the D_3 is increased. Therefore, this work may provide insights into the gas storage and seepage capabilities of coalbed methane (CBM) reservoirs, and thus will be favorable for enhancing CBM recovery.

Keywords: coals; scale-span pore structure; FIB-SEM tomography; X-ray μ-CT; 3D fractal dimension

1. Introduction

With increasing global demand for energy resources, coalbed methane (CBM) stored in coal seam has been paid considerable attention due to its triple play of mining safety, environment amity, and economical energy in recent years (Karacan et al., 2011; Vishal et al., 2015; Zhou et al., 2018). Coal is usually characterized as a dual-pore system, including matrix pores and cleat systems (macropores and fractures) (Clarkson and Bustin, 1999; Gan et al., 1972; Warren and Root, 1963). About 95% of the adsorbed gas is stored in the matrix pores of the coal. The cleat system is considered to be essential channels of gas and water output (Liu et al., 2017; Pillalamarry et al., 2011; Weishauptová et al., 2004). The pore structure affects not only the gas flow but also the gas adsorption capability and gas storage capacity (Cai et al., 2013; Clarkson and Bustin, 1999; Crosdale et al., 1998; Liu et al., 2017; Weishauptová et al., 2004; Zheng et al., 2018). The conventional reservoirs (such as sandstone reservoirs) are characterized by micro-scale pores, whereas nano-scale pores usually dominate coal reservoirs (Jiao et al., 2014; Tang et al., 2016). Therefore, the nano-scale pores are of great significance for understanding CBM adsorption and CBM resource assessment.

Experimental works have demonstrated that coal can have a range of pore sizes and a complex pore size distribution (Gan et al., 1972) through multiple techniques including transmission electron microscope (TEM) and field emission scanning electron microscope (FE-SEM) (Pan et al., 2016), mercury intrusion porosimetry (MIP) (Rigby et al., 2008) and nuclear magnetic resonance (NMR) (Zheng et al., 2018); N_2 low-pressure adsorption (Cai et al., 2018) and CO_2 adsorption (Mastalerz et al., 2012); small-angle neutron scattering (SANS) (Sakurovs et al., 2018) and small-angle X-ray scattering(SAXS) (Okolo et al., 2015). The above techniques mainly

focused on the comprehensive pore characteristics of entire coal core while lacking of the information for realistic pore networks. Therefore, evaluating and quantifying realistic pore-throat characteristic including distribution, location and orientation as well as mineral morphology remain an ongoing challenge, which is worthwhile devoting more efforts. In recent years, reconstructing 3D pore structures has emerged as an exciting technique (Balucan et al., 2018; Fang et al., 2019; Liu et al., 2017; Mathews et al., 2017; Saif et al., 2017).

For 3D characterization of pore structure, two favorite techniques which can offer 3D parameters of unconventional reservoir (e.g., shale and coal) at high resolution are focused ion beam-scanning electron microscopy (FIB-SEM) and X-ray computed micro-tomography (X-ray μ-CT) (Hemes et al., 2015; Liu et al., 2017; Saif et al., 2017; Silin and Kneafsey, 2012). 3D pore structure by FIB-SEM measurement has not been efficiently reported, especially for pores with diameter < 100 nm, which is of great significance for CBM adsorption, desorption and diffusion (Cai et al., 2013). FIB-SEM combines the imaging capabilities of the SEM with the precise milling and cross-section capability of a FIB. For the regions of interest, the sample can be serially sliced to produce a high-resolution of 10~20 nm/pixel (Wargo et al., 2013) (~10nm/pixel in this article). For X-ray μ-CT, previous researchers found that X-ray μ-CT could effectively and non-destructively acquire the fracture/cleat density, cleat surface morphology and the pore space (Saif et al., 2017). However, due to image resolution limitations, X-ray μ-CT may only show the ~~macropore~~ micro-scale pore 3D structure characteristics rather than nano-scale pores or gas adsorption space. The pore structure heterogeneity in coals possibly affects the macro-heterogeneity of the CBM reservoir, thus affecting the storage, seepage, and output of CBM (Zheng et al., 2018). For instance, the effects of pores on gas adsorption and seepage can be

assessed by the pore fractal characteristics at different sizes (Cai et al., 2013; Peng et al., 2017). Moreover, the seepage-pores contribution on core permeability can be evaluated by using classic geometry and thermodynamics fractal model (Peng et al., 2017). Besides, Nakagawa et al. (2000), Okolo et al. (2015) and Sakurovs et al. (2012) utilized SAXS and SANS techniques to acquire the fractal characteristics and pore size distribution, respectively. X-ray μCT technique has been successfully used to evaluate pore and fracture heterogeneity of different rank coals (Li et al., 2017). Normally, the fractal theory is an efficient way to quantitively assess the irregularity of coal surface based on scanning electron microscopy and low-temperature nitrogen adsorption (Liu and Nie, 2016). However, a few studies were conducted on the spatial heterogeneity of the pore network by using the box-counting method (Russell et al., 1980). Previous studies (Krohn and Thompson, 1986; Liu and Nie, 2016) also confirmed that the fractal dimension by the box-counting method can be adequately used to characterize the heterogeneity of coal pore distribution. Therefore, the box-counting method was adopted to characterize the 3D pore heterogeneity in this study.

In this work, a combined pore size classification of super micropores (< 2 nm), micropores (2-10 nm), mesopores (10-10^2 nm), macropores (10^2-10^3 nm), super macropores (10^3-10^4 nm) and micro-fractures (> 10^4 nm) from our previous research (Cai et al., 2013) will be adopted. We combine FIB-SEM and X-ray μCT techniques to evaluate the nano-microscale pore structure combined with fractal analysis. Firstly, the pore networks are established to evaluate the differences in nano and microstructure characteristics with the data of porosity, pore counts, pore area and pore volume. Secondly, the pore network model (PNM) is established by Avizo software to describe and quantify the pore throat. Additionally, with the obtained high-resolution FIB-SEM and

X-ray μCT images, the fractal analysis is conducted by using the box-counting method. Finally, the 3D pore network can be quantitatively evaluated. Therefore, this work may benefit the understanding of the complex structure of nano-micro scale pore that affecting gas storage and seepage capabilities, and also will be conducive to CBM reservoir improvement.

2. Samples and methodology

2.1. Sample preparation and basic information

Two coal samples were collected from the Liu Huanggou block of the southern Junggar Basin (LHG, 0.98% $R_{o,m}$) and the Zhengzhuang block of the southern Qinshui basin (L-1, 2.73% $R_{o,m}$), China. Measurements of maximum vitrinite reflectance ($R_{o,m}$) (immersion in oil) and maceral composition were conducted with a microscope photometer (MPV-III, Leitz Company of Germany) as in our previous research (Cai et al., 2018). An automatic proximate analyzer 5E-MACIII was used to analyze the moisture, ash yield, volatile matter, and fixed carbon contents. Table 1 shows the $R_{o,m}$, maceral composition, and the proximate analysis of the coals. The maximum vitrinite reflectance in oil immersion ($R_{o,m}$) of the two coals is 0.98% and 2.73% that belongs to the high-volatile bituminous coal and anthracite respectively, the coal composition of which varies markedly as shown in Table 1. Macerals are mainly composed of vitrinite of 53.40% and 66.80%, part of inertinite of 19.70% and 14.40%, less exinite of 0.37% and 0% and well-developed minerals of 26.50% and 18.80% for sample LHG and sample L-1 , respectively. The proximate analysis shows that the LHG and L-1 coals are having of 35.63% and 17.33% ash yields, and 0.76% and 7.71% moisture contents respectively.

2.2. Methodologies for FIB-SEM and X-ray μ-CT

Before FIB-SEM imaging, sample preparation was firstly performed. Two cubic samples of ~ 0.5

cm × 1 cm × 1 cm were polished using dry emery paper to form a flat surface (as shown in Fig. 1), which was then polished by argon ions. The polished coal samples were dried for 12 h at 65 ℃ and then coated with carbon. These two samples were then put into the Zeiss Crossbeam540 system for imaging. The area of the scanning area is approximately 10 μm × 10 μm. In the FIB-SEM experiment, the cutting of the focused ion beam is performed simultaneously with the imaging of the scanning electron microscope. The acceleration voltage is 1kV during the experiment, the current is 0.8 nA, and the test time is 10 hours. A thousand SEM images of each coal obtained with resolution of ~10 nm were used to describe the pore network.

Before performing the X-ray μ-CT scanning measurements, two coal pillars with a diameter of ~1.0 mm and a height of ~2.0 mm were first drilled. The scan was then carried out using a Nano Voxel-3000 X-ray 3D microscope with a 20x lens detector (Sanying Precision Instruments Co., Ltd., China). The scanning area of X-ray μ-CT was a columnar region having a diameter of ~1 mm and a height of ~1 mm. The experimental conditions were a voltage of 80 kV and a current of 95 μA. Finally, each 3D data set of the two samples includes more than 1000 CT scan images. The resolutions of the samples LHG and L-1 were 0.55 μm and 0.63 μm, respectively. The data obtained from both experiments were stacked and analyzed by Avizo software as our previous study (Li et al., 2017). The porosity was calculated by the *volume fraction* module in Avizo software.

2.3. Fractal analysis in coals

Fractal geometry was proposed by Benoit Mandelbrot in 1982, which can be used to effectively characterize the heterogeneity of pore structure in porous media with fractal dimension (Mandelbrot, 1983). The larger the fractal dimension is, the stronger heterogeneity of the pore

structure is (Reich et al., 1992). In this work, the fractal dimension was used as the evaluation parameter of heterogeneity. Fractal dimension of pore structure can be determined by the data from mercury intrusion porosimetry (Peng et al., 2017), low-temperature nitrogen adsorption (Mahnke and Mögel, 2003) and related images (e.g. SEM images and CT images) (Liu and Nie, 2016; Wu et al., 2019). Several methods based on image calculation (Krohn and Thompson, 1986; Lopes and Betrouni, 2009; Russell et al., 1980) were proposed including the box-counting method, fractional Brownian motion method and area measurement method. In this study, the popular box-counting method will be utilized. The main principle is as follows:

Firstly, let A be any non-empty bounded subset of the space R^n. If ~~For any~~ $\delta > 0$, $N_\delta(\mathrm{A})$ represents the minimum number of n-dimensional boxes with a side length δ required to cover A. When $\delta \to 0$, a relationship exists:

$$N_\delta(\mathrm{A}) \propto \delta^{-D} \tag{1}$$

Where D is the fractal dimension of space A. And when there is only one k, there is:

$$\lim_{\delta \to 0} \frac{N_\delta(\mathrm{A})}{\delta^{-D}} = k \tag{2}$$

Take the logarithm of both sides of the equation at the same time, we can acquire:

$$\lim_{\delta \to 0} (\log N_\delta(\mathrm{A}) + D \log \delta) = \log k \tag{3}$$

Which can be a substitute as:

$$D = \lim_{\delta \to 0} \frac{\log k - \log N_\delta(\mathrm{A})}{\log \delta} = -\lim_{\delta \to 0} \frac{\log N_\delta(\mathrm{A})}{\log \delta} \tag{4}$$

The side length δ_i of the box takes a series of values and counts the number $N_{\delta_i}(\mathrm{A})$ of boxes required to cover A. The $[\log \delta_i, \log N_{\delta_i}(\mathrm{A})]$ line is drawn in the coordinate system with $\log \delta$ as the abscissa and $\log N_{\delta_i}(\mathrm{A})$ as the ordinate. The straight line is fitted by the least square method, and the slope is the fractal dimension D.

In this work, the 3D fractal dimension (D_3) and 2D fractal dimension (D_2) are calculated based on high-resolution FIB-SEM and CT images. In the above algorithm, A is a binarized high-resolution FIB-SEM/CT image with side length of $M \times M$ or $M \times M \times M$. If A cannot be divided by the box with the side length δ, the box-counting method will produce areas smaller than $\delta \times \delta$ (or $\delta \times \delta \times \delta$) at the edge of the image. The information contained in these areas will be ignored during the calculation process, which is the boundary effect. To avoid the loss of image information, the common factor of the length and width of the original image is taken as the side length of a series of boxes (Wu et al., 2019). Noise will be generated due to the volatility of the incident electrons during the imaging process. Therefore, the images should be denoised first by the median filtering method. Then, the threshold is determined for the binarized image with the commonly used Otsu algorithm (i.e., the global threshold method) due to its high efficiency, conciseness and remarkable effect (Otsu, 1979; Prakongkep et al., 2010; Zhou and Xie, 2003). Finally, fractal dimension of pores is calculated by the box-counting method. The 3D analysis was conducted with the voxels of 500 × 500 × 500 when calculating spatial fractal D_3. Due to the limitation of the computer's operating performance (the larger the size, the better the computer's operating performance is needed), and the need to avoid the impact of other variables caused by the different sizes, so the size of the selected region is 500 × 500 × 500 voxels. Besides, the size of 500 × 500 × 500 voxels is sufficient for evaluating the heterogeneity of the pore network in coal samples. To eliminate the inaccurate result caused by the different initialization positions, the domain of the 3D model constructed by different cubes is initialized from 9 locations of eight vertices and the center point of the cube. The size of the cube grows by 10 pixels per time. In other words, if there is a cube with a side length of 500, a total of 450 cubes of different side lengths

will be produced in 9 different directions. Due to nine cubes are identical, the original cube with a side length of 500 will be divided into 442 different cubes. The average value of the nine directions is deemed as the D_3 of the fractal spatial pore structure of the various box size. Simultaneously, the the 2D fractal dimension of the cube with different sizes is also assessed . Combining the above theories, the box-counting method is automatically programmed based on Matlab software to calculate the fractal dimension. In this work, the spatial fractal of D_3 for pore structure of coals will be discussed in detail.

3. Results and Discussions

3.1. Pore-fracture in 2D morphology

The pore size, type, and structure of coal reservoirs are extremely inconsistent due to the fundamental differences in plant remains and a series of changes in the process of coalification. In this study, the pore morphology, structure, and distribution of selected coal samples were qualitatively described by the argon-ion polishing-SEM technique. Based on pore genesis and distribution characteristics, matrix pores in coal can be divided into two main types: (1) organic matter (OM) pores, including stomas and shrinkage pores; and (2) mineral associated (MA) pores, including intragranular pores in minerals and intergranular pores between crystals and matrix (Loucks et al., 2012). Using argon-ion polishing-SEM images, it was found that a wide variety of OM pores and MA pores were developed in the two coal samples, and some micro-scale fractures existed (Figs. ~~1~~ 2 and ~~2~~3). For the high volatile bituminous coal (sample LHG), a large amount of gas is produced in the early stage of coalification, and the shapes of pores are mostly round with a smooth edge. However, due to the higher pressure of the overburden, the pores are compressed, thereby exhibiting various irregular shapes (including slit-like and wedge shape, as shown in Fig.

2~~1~~) and exhibiting a clear directional arrangement (Fig. 2~~1~~c). Meanwhile, due to the compression and destruction of the overburden pressure, some of the pores appear connected. Besides, some of the pores are accompanied by the phenomenon of being filled with minerals (Fig. 2~~1~~e). Clustered pores are visible in some areas (Fig. 2~~1~~f). As the coalification progresses, a large number of pores are formed in the anthracite L-1, which are round or other irregular shapes and are present in clusters in the coal matrix (~~Fig. 2~~Fig. 3f). Some pores and fractures are filled with minerals (~~Fig. 2~~Fig. 3a-d). Due to fluid erosion, there are erosive pores in the sample (~~Fig. 2~~Fig. 3e).

3.2. Quantitative 3D pore networks

~~Fig. 3~~Fig. 4 shows 3D reconstruction images (a_1-d_1) and corresponding pore network (a_2-d_2) extracted with Avizo software. In the images on the left, black is pore-fracture, gray is coal matrix and white is mineral. On the right, blue is the extracted pore network. Both reconstruction blocks have a dimension of 10 μm × 10 μm × 10 μm by FIB-SEM data. The data volume sizes of the X-ray μCT experiments are 275 μm × 275 μm × 275 μm and 315 μm × 315 μm × 315 μm, respectively. For the FIB-SEM experimental data set, the area of characterization is small and the computer running performance is not high when the algorithm is running. Therefore, the 1000 slices obtained from the experiment were applied to 3D reconstruction to completely restore the pore network characteristics at the nanoscale. For the CT experiment, the area of its characterization is relatively large, and the data set of more than 1000 slices is too high for computer performance. Therefore, the uniform characterization size selected here is 500 × 500 × 500 voxels, which can better display the three-dimensional distribution characteristics of the pore network at the micrometer scale. Quantitative characterization of the pore network was performed by the Avizo software , as shown in Table 2. The porosities of sample LHG and sample L-1 at

different scales were 5.23% and 1.06% for FIB-SEM, 20.41% and 8.67% for X-ray μCT, respectively. The mesopores are the most developed in FIB-SEM data, while the macropores and super-macropores are extensive development in the CT data, resulting in the calculated porosity of the FIB-SEM data in the same sample being lower than that calculated from the CT data. ~~Fig. 4~~Fig. 5 shows the 3D spatial distribution of the pore network in different ranges of the two samples~~. Fig. 4~~ and suggests that the 3D spatial pore network has obvious heterogeneity. Besides, X-ray μCT shows a larger number of pore-fractures than the FIB-SEM. The FIB-SEM data for LHG and L-1 in Table 2 showed the pore numbers of 36712 and 11762, the total pore areas of 2105.45 μm^2 and 515.33 μm^2, and the total pore volumes of 51.63 μm^3 and 10.56 μm^3, respectively. This result indicates that the LHG can provide more storage volume for methane than that of the L-1. The X-ray μCT data for LHG and L-1 showed the pore numbers of 180977 and 198822, the total pore area of 8685787.31 μm^2 and 5760660.30 μm^2, and the total pore volume of 4114728.90 μm^3 and 2354981.18 μm^3, respectively. And the two samples have well developed 2811 and 177 micro-fractures respectively, which should be the essential seepage channel for CBM. In other words, LHG has a better percolation ability than the sample L-1. ~~Fig. 5~~Fig. 6 depicts the pore distribution and volume percentage in different ranges. For the FIB-SEM (~~Fig. 5~~Fig. 6a and 6~~5~~c), the pore sizes exhibit bimodal distribution. The peaks of LHG and L-1 are located at 10 nm - 20 nm and 300 nm - 500 nm, 20 nm - 30 nm and 300 nm - 500 nm, respectively. Also, in the two samples, the pores with the range of 300-500 nm contributed the most to the porosity at the nanometer scale. For the X-ray μCT, the pore size distribution of the LHG presents a three-peak characteristic (~~Fig. 5~~Fig. 6b) with three peaks around 0.5 μm - 0.7 μm, 1 μm - 2 μm and 9 μm - 10 μm. Moreover, the pores with sizes of 1 μm - 2 μm, 11 μm - 12 μm, 15 μm - 20 μm contribute

more to the microscale porosity. The pore size distribution of L-1 shows a bimodal structure (~~Fig.~~ ~~5~~Fig. 6d) with two peaks at 0.7 μm - 0.9 μm and 1 μm - 2 μm. And the pores of 3 μm - 4 μm contribute most to microscale porosity.

The pore networks are established with the Avizo software , and the 3D pore throat structures are displayed and quantified as shown in ~~Fig. 6~~Fig. 7 and Table 3. The two FIB-SEM data volumes used here is still 10 μm × 10 μm × 10 μm. With the X-ray μCT data, the analyzed volumes were 110 μm × 110 μm × 110 μm for LHG and 126 μm ×126 μm ×126 μm for L-1. Because if the original voxel size is used, it is not conducive to further observation of pore throat characteristics. The analysis parameters including counts, area, average channel length, total channel length and volume vary markedly as shown in Table 3. The throats of the LHG are well developed as presented in ~~Fig. 6~~Fig. 7 a_1 and b_1, and the pore-fractures are well connected through the throat. Fig ~~6~~$a_2$7a_2, b_2 with Table 3 show that the pore throats in the range of 100 nm – 200 nm and 3000 nm – 4000 nm contribute the most to the seepage pore network of the LHG. In contrast, the throats of L-1 develop locally at the nanoscale as shown in Fig 7~~6~~c_1. ~~Fig. 6~~Fig. 7c_2 and Table 3 exhibit that the pore throats in the range of 100 nm – 200 nm dominate the seepage network of the L-1. However, L-1 develops fewer throats at the microscale as shown in ~~Fig. 6~~Fig. 7d, and the pores are isolated. Therefore~~,~~, the LHG should have a better permeability than that of L-1.

3.3. Pore heterogeneity by fractal dimension

The D_3 results calculated based on the box-counting method (Liu and Nie, 2016; Wu et al., 2019) are presented in ~~Fig. 7~~Fig. 8, which indicates that D_3 floats within a certain size range, but remains essentially unchanged if the calculation domain size exceeds a critical value. To determine the critical value, the first derivative by the function of D_3 varies with increasing computation domain

size was evaluated. The point that first approaches 0 after the first derivative undergoes a significant change is defined as a turning point, which is expressed as D_3 almost stops growing from this point. The critical value determined by the fractal dimension is referred to as the representative elementary volume (REV) (Wu et al., 2019), and the fractal dimension value of the REV will represent the fractal characteristics of the sample. As shown in ~~Fig. 7~~Fig. 8, the side lengths of the REVs of the four data sets (sample LHG of FIB-SEM, sample L-1 of FIB-SEM, samples LHG and L-1 of CT) are 80, 280, 100 and 100 pixels, the corresponding D_3 are 2.23, 2.04, 2.69 and 2.51, respectively. REVs demonstrate that the pore networks of the selected coals have self-similarity. Simultaneously, the spatial pore networks of the two coals are complex, and the heterogeneity of the LHG is stronger.

For the same coal, the FIB-SEM and the X-ray μ-CT images represent two different scales, that is, nanoscale and microscale. The image resolution of the FIB-SEM is 10 nm/pixel, and the image resolutions of the X-ray μ-CT are 0.55 μm/pixel for LHG and 0.63 μm / pixel for L-1, respectively. The smallest box size in the box-counting method is 100×100×100 nm^3 and 5.5/6.3×5.5/6.3×5.5/6.3 μm^3, respectively. ~~Fig. 7~~Fig. 8 shows the existence of REV at both the nanoscale and microscale; that is, the self-similarity pattern has been built at the nanoscale before the self-similar model is formed at the microscale. Therefore, the pore network is not an isolated development but a secondary development.

Besides, D_2 has a very significant linear relationship with D_3 as shown in ~~Fig. 8~~Fig. 9, which is very close to $D_3=D_2+1$ when the porosity is 100% as proven by Wu et al. (2019). The reason for some errors may be that the pore network-fracture system in the coal reservoir has mineral filling or sedimentation during development, which deviates from the original state. The realistic

relationship between the porosity and three-dimensional fractal dimension is shown in ~~Fig. 9~~Fig. 10, which may be due to the pore network in the coal reservoir having mineral filling. Therefore, two different trends have emerged. ~~Fig. 9~~Fig. 10b shows that the porosity increases with increasing D_3; that is, the porosity of L-1 in FIB-SEM increases as the spatial complexity of pore network increases. ~~Fig. 9~~Fig. 10a, c~~,~~ and d display that the porosity decreases with the increasing D_3. The positive trend should be closely related to the complex pore structure. The more complex the pore structure is, the higher the porosity is. The negative correlation should be contributed to a large amount of mineral filling pores. Pores filled with minerals will increase the proportion of small pores and decrease the porosity, which increases the spatial complexity of the pore networks. Therefore, the D_3 increases.

4. Conclusions

In this work, FIB-SEM and X-ray μCT techniques with fractal methods provided a synergistic multiscale and multidimensional evaluation of pore networks. The 3D pore networks and their quantitative analysis of the LHG and L-1 coals were carefully carried out. Additionally, the box-counting method is adopted to acquire the three dimensional complexity (D_3) of the pore networks, which can quantitatively evaluate the spatial structure of the pore networks. Moreover, factor affecting the complexity of the pore networks including minerals, pore size and porosity were found. Therefore, the following conclusions can be made:

1) With the images of FIB-SEM and X-ray μ-CT, the pore size distribution and porosity of the selected two coals at different scales is determined. The pore size distribution indicates that pores in the main size range of 300-500 nm, 1 μm – 2 μm, 11 μm – 12 μm, and 15 μm – 20 μm contribute significantly to the porosity of the LHG; for the L-1, pores in the range of 300-500 nm

and 3 μm – 4 μm contribute most to porosity, which vary markedly. The porosities of LHG and L-1 at different scales are 5.23% and 1.06% for FIB-SEM, 20.41% and 8.67% for X-ray μCT, respectively, which indicates that the LHG can provide more storage volume for CBM than that of the L-1.

2) The spatial pore networks and the pore throat are well established, which shows that the LHG has both well developed nanoscale and microscale pores. Whereas the L-1 locally develops a small number of throats at the nanometer scale, and no throat at the micrometer scale. Therefore, the LHG should have a better permeability than that of L-1.

3) Based on the box-counting method, D_3 values of four data sets (the LHG for FIB-SEM, the L-1 for FIB-SEM, the LHG for CT and the L-1 for CT) are 2.23, 2.04, 2.69 and 2.51, respectively, which demonstrates that the spatial pore networks of the selected coals have self-similarity with a secondary development. Porosity affecting the complexity of the pore networks was found that for the relationship between porosity and D_3, two opposite trends exist considering the complex pore structure and a large amount of mineral filling pores.

Acknowledgements

This research was funded by the National Natural Science Foundation of China (grant nos. 41830427, 41922016, and 41772160) and the Fundamental Research Funds for Central Universities (grant no. 2652018002).

References

Balucan, R.D., Turner, L.G., Steel, K.M., 2018. X-ray mu CT investigations of the effects of cleat

demineralization by HCl acidizing on coal permeability. J. Nat. Gas. Sci. Eng. 55, 206-218.

Cai, Y.D., Li, Q., Liu, D.M., Zhou, Y.F., Lv, D.W., 2018. Insights into matrix compressibility of coals by mercury intrusion porosimetry and N-2 adsorption. Int. J. Coal Geol. 200, 199-212.

Cai, Y.D., Liu, D.M., Pan, Z.J., Yao, Y.B., Li, J.Q., Qiu, Y.K., 2013. Pore structure and its impact on CH4 adsorption capacity and flow capability of bituminous and subbituminous coals from Northeast China. Fuel 103, 258-268.

Clarkson, C.R., Bustin, R.M., 1999. Effect of pore structure and gas pressure upon the transport properties of coal: a laboratory and modeling study. 1. Isotherms and pore volume distributions. Fuel 78, 1333-1344.

Crosdale, P.J., Beamish, B.B., Valix, M., 1998. Coalbed methane sorption related to coal composition. Int. J. Coal Geol. 35, 147-158.

Fang, H.H., Sang, S.X., Liu, S.Q., Du, Y., 2019. Methodology of three-dimensional visualization and quantitative characterization of nanopores in coal by using FIB-SEM and its application with anthracite in Qinshui basin. J. Pet. Sci. Eng. 182, 1-11.

Gan, H., Nandi, S.P., Walker Jr, P.L., 1972. Nature of the porosity in American coals. Fuel 51, 272-277.

Hemes, S., Desbois, G., Urai, J.L., Schröppel, B., Schwarz, J.-O., 2015. Multi-scale characterization of porosity in Boom Clay (HADES-level, Mol, Belgium) using a combination of X-ray μ-CT, 2D BIB-SEM and FIB-SEM tomography. Micropor. Mesopor. Mat. 208, 1-20.

Jiao, K., Yao, S.P., Liu, C., Gao, Y.Q., Wu, H., Li, M.C., Tang, Z.Y., 2014. The characterization and quantitative analysis of nanopores in unconventional gas reservoirs utilizing FESEM-FIB and image processing: An example from the lower Silurian Longmaxi Shale, upper Yangtze region, China. Int. J. Coal Geol. 128, 1-11.

Karacan, C.Ö., Ruiz, F.A., Cote, M., Phipps, S., 2011. Coal mine methane: A review of capture and utilization practices with benefits to mining safety and to greenhouse gas reduction. Int. J. Coal Geol. 86, 121-156.

Krohn, C.E., Thompson, A.H., 1986. Fractal Sandstone Pores - Automated Measurements Using Scanning-Electron-Microscope Images. Phys. Rev B. 33, 6366-6374.

Li, Z.T., Liu, D.M., Cai, Y.D., Ranjith, P.G., Yao, Y.B., 2017. Multi-scale quantitative characterization of 3-D pore-fracture networks in bituminous and anthracite coals using FIB-SEM tomography and X-ray mu-CT. Fuel 209, 43-53.

Liu, S.Q., Sang, S.X., Wang, G., Ma, J.S., Wang, X., Wang, W.F., Du, Y., Wang, T., 2017. FIB-SEM and X-ray CT characterization of interconnected pores in high-rank coal formed from regional metamorphism. J. Pet. Sci. Eng. 148, 21-31.

Liu, X.F., Nie, B.S., 2016. Fractal characteristics of coal samples utilizing image analysis and gas adsorption. Fuel 182, 314-322.

Lopes, R., Betrouni, N., 2009. Fractal and multifractal analysis: A review. Med. Image. Anal. 13, 634-649.

Loucks, R.G., Reed, R.M., Ruppel, S.C., Hammes, U., 2012. Spectrum of pore types and networks in mudrocks and a descriptive classification for matrix-related mudrock pores. AAPG Bull. 96, 1071-1098.

Mahnke, M., Mögel, H.J., 2003. Fractal analysis of physical adsorption on material surfaces. Colloids. Surfaces. A. 216, 215-228.

Mandelbrot, B.B., 1983. The Fractal Geometry of Nature. Sciences 23, 63-68.

Mastalerz, M., He, L., Melnichenko, Y.B., Rupp, J.A., 2012. Porosity of Coal and Shale: Insights from

Gas Adsorption and SANS/USANS Techniques. Energ. Fuel. 26, 5109-5120.

Mathews, J.P., Campbell, Q.P., Xu, H., Halleck, P., 2017. A review of the application of X-ray computed tomography to the study of coal. Fuel 209, 10-24.

Nakagawa, T., Komaki, I., Sakawa, M., Nishikawa, K., 2000. Small angle X-ray scattering study on change of fractal property of Witbank coal with heat treatment. Fuel 79, 1341-1346.

Okolo, G.N., Everson, R.C., Neomagus, H.W.J.P., Roberts, M.J., Sakurovs, R., 2015. Comparing the porosity and surface areas of coal as measured by gas adsorption, mercury intrusion and SAXS techniques. Fuel 141, 293-304.

Otsu, N., 1979. A Threshold Selection Method from Gray-Level Histograms. IEEE . T. Syst. Man. Cy. 9, 62-66.

Pan, J., Wang, K., Hou, Q., Niu, Q., Wang, H., Ji, Z., 2016. Micro-pores and fractures of coals analysed by field emission scanning electron microscopy and fractal theory. Fuel 164, 277-285.

Peng, C., Zou, C.C., Yang, Y.Q., Zhang, G.H., Wang, W.W., 2017. Fractal analysis of high rank coal from southeast Qinshui basin by using gas adsorption and mercury porosimetry. J. Pet. Sci. Eng. 156, 235-249.

Pillalamarry, M., Harpalani, S., Liu, S.M., 2011. Gas diffusion behavior of coal and its impact on production from coalbed methane reservoirs. Int. J. Coal Geol. 86, 342-348.

Prakongkep, N., Suddhiprakarn, A., Kheoruenromne, I., Gilkes, R.J., 2010. SEM image analysis for characterization of sand grains in Thai paddy soils. Geoderma 156, 20-31.

Reich, M.H., Snook, I.K., Wagenfeld, H.K., 1992. A fractal interpretation of the effect of drying on the pore structure of Victorian brown coal. Fuel 71, 669-672.

Rigby, S.P., Chigada, P.I., Evbuomvan, I.O., Chudek, J.A., Miri, T., Wood, J., Bakalis, S., 2008.

Experimental and modelling studies of the kinetics of mercury retraction from highly confined geometries during porosimetry in the transport and the quasi-equilibrium regimes. Chem. Eng. Sci. 63, 5771-5788.

Russell, D.A., Hanson, J.D., Ott, E., 1980~~b~~. Dimension of strange attractors. Phys. Rev. Lett. 45, 1175–1178.

Saif, T., Lin, Q.Y., Butcher, A.R., Bijeljic, B., Blunt, M.J., 2017. Multi-scale multi-dimensional microstructure imaging of oil shale pyrolysis using X-ray micro-tomography, automated ultra-high resolution SEM, MAPS Mineralogy and FIB-SEM. Appl. Energ. 202, 628-647.

Sakurovs, R., He, L.L., Melnichenko, Y.B., Radlinski, A.P., Blach, T., Lemmel, H., Mildner, D.F.R., 2012. Pore size distribution and accessible pore size distribution in bituminous coals. Int. J. Coal Geol. 100, 51-64.

Sakurovs, R., Koval, L., Grigore, M., Sokolova, A., Ruppert, L.F., Melnichenko, Y.B., 2018. Nanometre-sized pores in coal: Variations between coal basins and coal origin. Int. J. Coal Geol. 186, 126-134.

Silin, D., Kneafsey, T., 2012. Shale Gas: Nanometer-Scale Observations and Well Modelling. J. Can. Petrol. Technol. 51, 464-475.

Tang, X.L., Jiang, Z.X., Jiang, S., Li, Z., 2016. Heterogeneous nanoporosity of the Silurian Longmaxi Formation shale gas reservoir in the Sichuan Basin using the QEMSCAN, FIB-SEM, and nano-CT methods. Mar. Petrol. Geol. 78, 99-109.

Vishal, V., Singh, T.N., Ranjith, P.G., 2015. Influence of sorption time in CO2-ECBM process in Indian coals using coupled numerical simulation. Fuel 139, 51-58.

Wargo, E.A., Kotaka, T., Tabuchi, Y., Kumbur, E.C., 2013. Comparison of focused ion beam versus

nano-scale X-ray computed tomography for resolving 3-D microstructures of porous fuel cell materials. J. Power. Sources. 241, 608-618.

Warren, J.E., Root, P.J., 1963. The Behavior of Naturally Fractured Reservoirs. SPE-426-PA 3, 245-255.

Weishauptová, Z., Medek, J., Kovář, L., 2004. Bond forms of methane in porous system of coal II. Fuel 83, 1759-1764.

Wu, H., Zhou, Y.F., Yao, Y.B., Wu, K.J., 2019. Imaged based fractal characterization of micro-fracture structure in coal. Fuel 239, 53-62.

Zheng, S.J., Yao, Y.B., Liu, D.M., Cai, Y.D., Liu, Y., 2018. Characterizations of full-scale pore size distribution, porosity and permeability of coals: A novel methodology by nuclear magnetic resonance and fractal analysis theory. Int. J. Coal Geol. 196, 148-158.

Zhou, H.W., Xie, H., 2003. Direct estimation of the fractal dimensions of a fracture surface of rock. Surf. Rev. Lett. 10, 751-762.

Zhou, H.W., Zhong, J.C., Ren, W.G., Wang, X.Y., Yi, H.Y., 2018. Characterization of pore-fracture networks and their evolution at various measurement scales in coal samples using X-ray mu CT and a fractal method. Int. J. Coal Geol. 189, 35-49.

Captions for Figures and Tables

Fig. 1. Pictures of samples used in FIB-SEM experiments. (a) is a front view and (b) is a top view.

Fig. ~~1~~2. The pore-fracture morphology of the sample LHG. (a) and (b) observe the pore-fracture distribution and morphology of the sample from a large viewing angle. (c) exhibits a directional alignment and some irregularly shaped pores; (d) shows irregular pores; (e) presents the phenomenon of mineral filling and partially connected pores; (f) shows the clustered pores.

~~Fig. 2~~Fig. 3. The pore-fracture morphology of the sample L-1. (a) and (b) observe the fractures distribution, morphology and some fractures filled with mineral. (c) and (d) exhibits pores of different shapes and filled with mineral; (e) presents fluid erosion pores; (f) shows the clustered pores.

~~Fig. 3~~Fig. 4. 3D reconstruction images (a_1-d_1) and corresponding extracted pore-fracture system (a_2-d_2) by Avizo2019 : (a_1), (a_2) - FIB-SEM data of sample LHG; (b_1), (b_2) - X-ray μCT data of sample LHG; (c_1), (c_2) - FIB-SEM data of sample L-1; (d_1), (d_2) - X-ray μCT data of sample L-1. In the images on the left, black is pore-fracture, gray is the coal matrix, and white is mineral. On the right, blue is the extracted pore network.

~~Fig. 4~~Fig. 5. 3D spatial distribution of pore-fraction system in different ranges. a_1-a_3: FIB-SEM data of sample LHG; b_1-b_3: X-ray μCT data of sample LHG; c_1-c_3: FIB-SEM data of sample L-1; d_1-d_3: X-ray μCT data of sample L-1.

~~Fig. 5~~Fig. 6. Histogram depicting results of pore distribution and volume percentage in different ranges. (a): FIB-SEM data of sample LHG; (b): X-ray μCT data of sample LHG; (c): FIB-SEM data of sample L-1; (d): X-ray μCT data of sample L-1.

~~Fig. 6~~Fig. 7. Pore network model showing 3D pore-throat skeletal structure and distribution of throats. a_1-a_2: FIB-SEM data of sample LHG; b_1-b_2: X-ray μCT data of sample LHG; c_1-c_2: FIB-SEM data of

sample L-1; d: X-ray μCT data of sample L-1.

~~Fig. 7~~Fig. 8. The relationship between the three-dimensional fractal dimension (D_3) and box size. (a_1) - (d_1) is the trend of D_3 with the box size. It indicates that D_3 floats within a certain size range, but remains essentially unchanged if the calculation domain size exceeds a critical value. (a_2) - (d_2) is the first derivative of the left curve, which is used to characterize the rate of change of D_3. The point that first approaches 0 after the first derivative undergoes a significant change is defined as a turning point, which is expressed as D_3 almost stops growing from this point.

~~Fig. 8~~Fig. 9 The relationship between two-dimensional (D_2) fractal dimension and three-dimensional fractal dimension (D_3). It is found that the two-dimensional fractal dimension has a very significant linear relationship with the three-dimensional fractal dimension.

~~Fig. 9~~Fig. 10. Relationship between three-dimensional fractal dimension and porosity. (b) shows that the porosity increases with increasing D_3; that is, the porosity of sample L-1 increases as the three-dimensional spatial distribution complexity of pore-fracture system increases. (a) (c) and (d) display that the porosity decreases with the rise of D_3.

Table 1 Sample information and basic parameters of the selected Chinese coals

Table 2 Pore size distribution characteristics of the pore-fracture system for the selected coals

Table 3 Pore throat parameter information calculated by the PNM module in Avizo

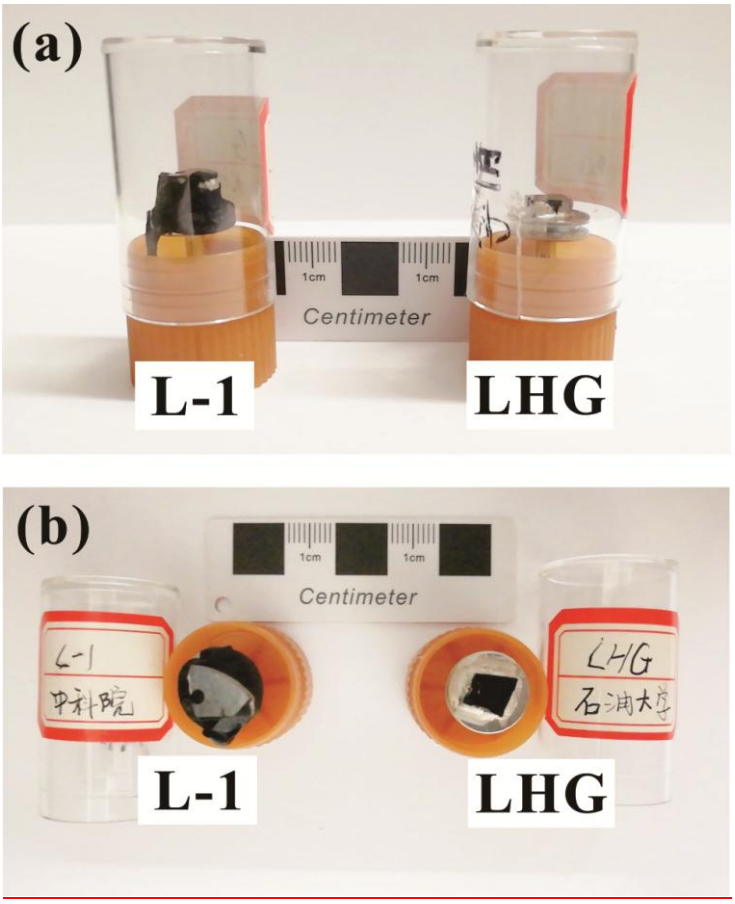

Fig. 1. Pictures of samples used in FIB-SEM experiments. (a) is a front view and (b) is a top view.

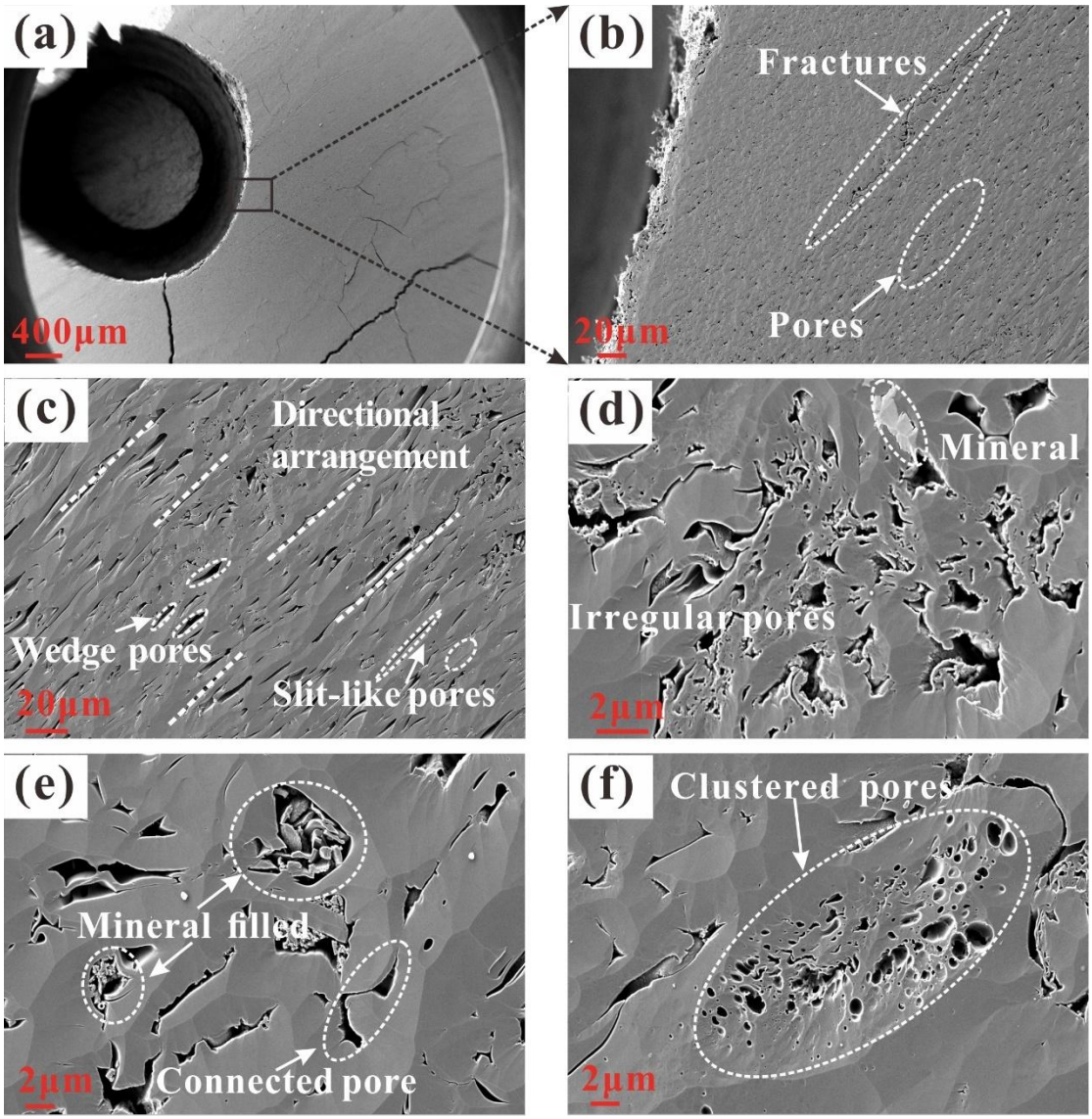

Fig. ~~1~~2. The pore-fracture morphology of the sample LHG. (a) and (b) observe the pore-fracture distribution and morphology of the sample from a large viewing angle. (c) exhibits a directional alignment and some irregularly shaped pores; (d) shows irregular pores; (e) presents the phenomenon of mineral filling and partially connected pores; (f) shows the clustered pores.

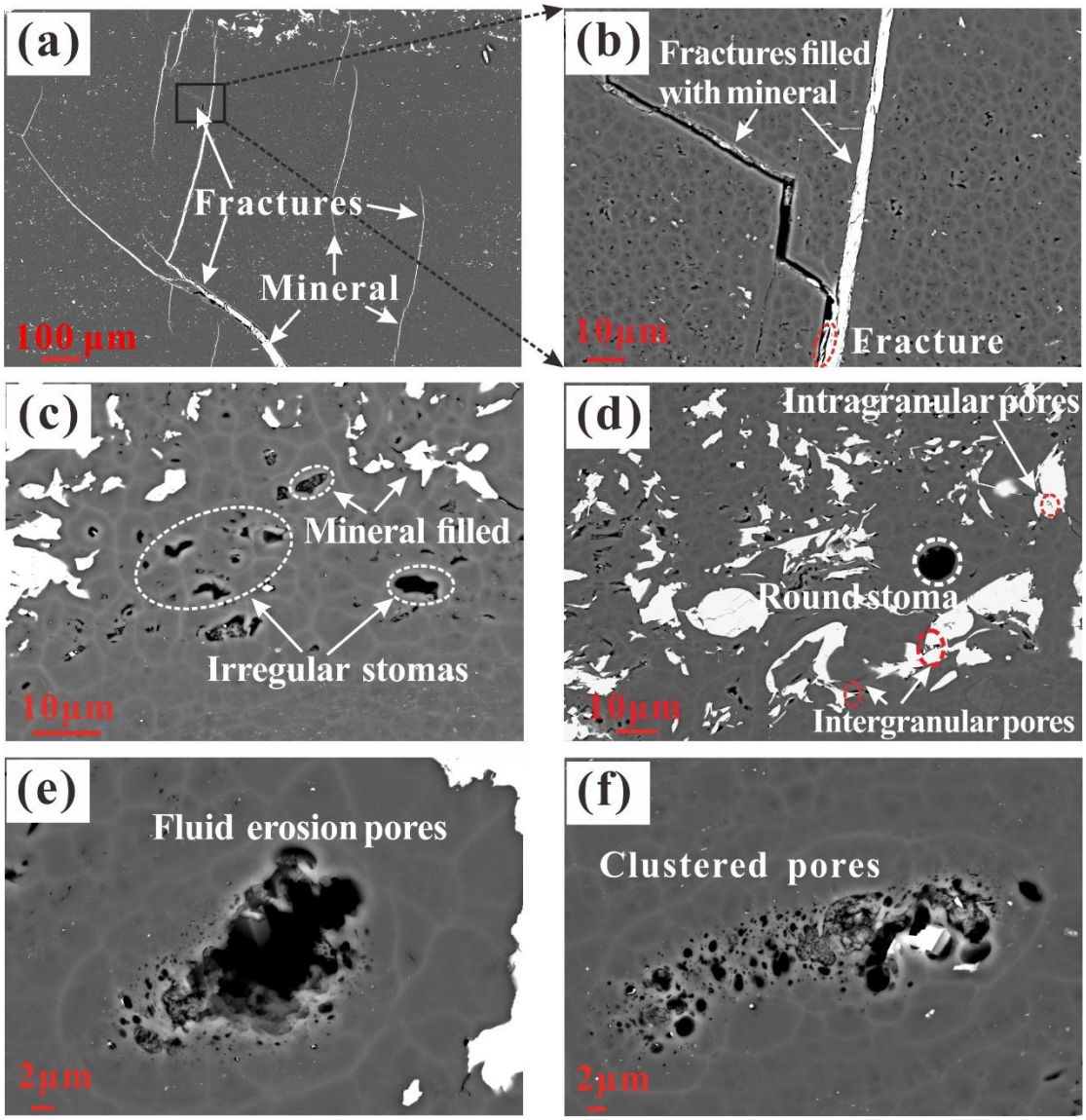

499

500 ~~Fig. 2~~Fig. 3. The pore-fracture morphology of the sample L-1. (a) and (b) observe the fractures distribution,

501 morphology and some fractures filled with mineral. (c) and (d) exhibits pores of different shapes and filled with

502 mineral; (e) presents fluid erosion pores; (f) shows the clustered pores.

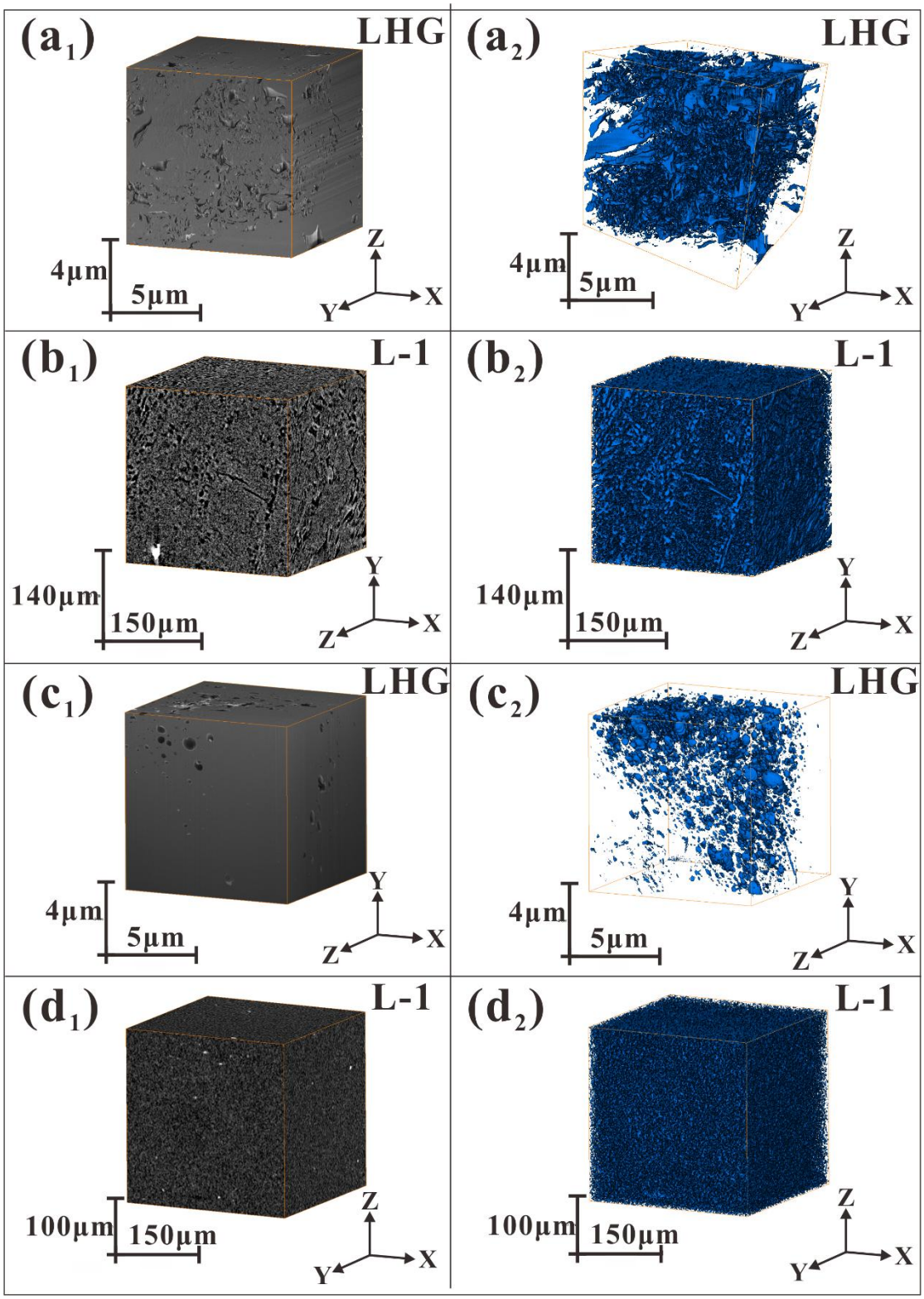

~~Fig. 3~~Fig. 4. 3D reconstruction images (a_1-d_1) and corresponding extracted pore-fracture system (a_2-d_2) by Avizo2019 : (a_1), (a_2) - FIB-SEM data of sample LHG; (b_1), (b_2) - X-ray μCT data of sample LHG; (c_1), (c_2) - FIB-SEM data of sample L-1; (d_1), (d_2) - X-ray μCT data of sample L-1. In the images on the left, black is pore-fracture, gray is the coal matrix, and white is mineral. On the right, blue is the extracted pore network.

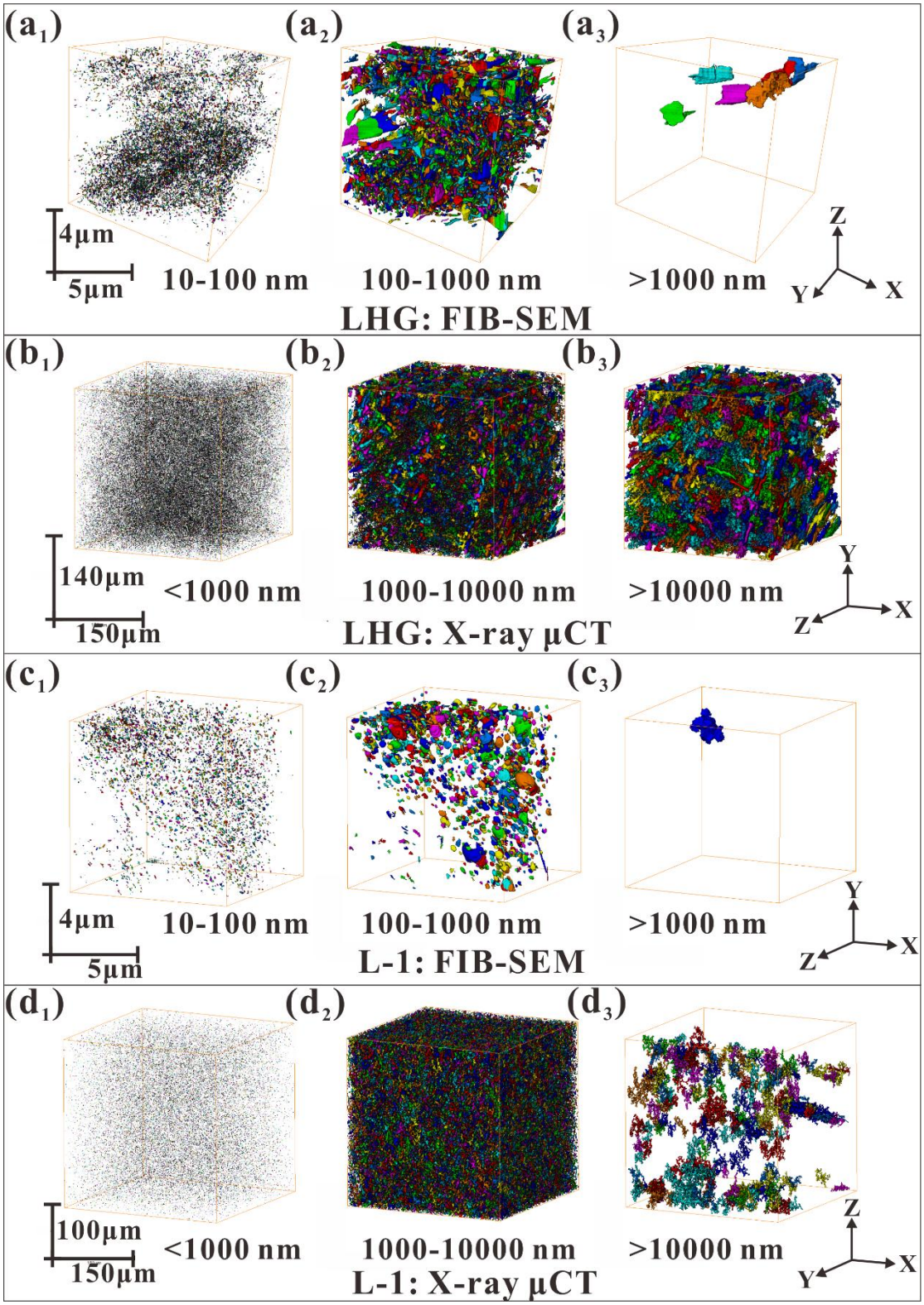

~~Fig. 4~~Fig. 5. 3D spatial distribution of pore-fraction system in different ranges. a_1-a_3: FIB-SEM data of sample LHG; b_1-b_3: X-ray μCT data of sample LHG; c_1-c_3: FIB-SEM data of sample L-1; d_1-d_3: X-ray μCT data of sample L-1.

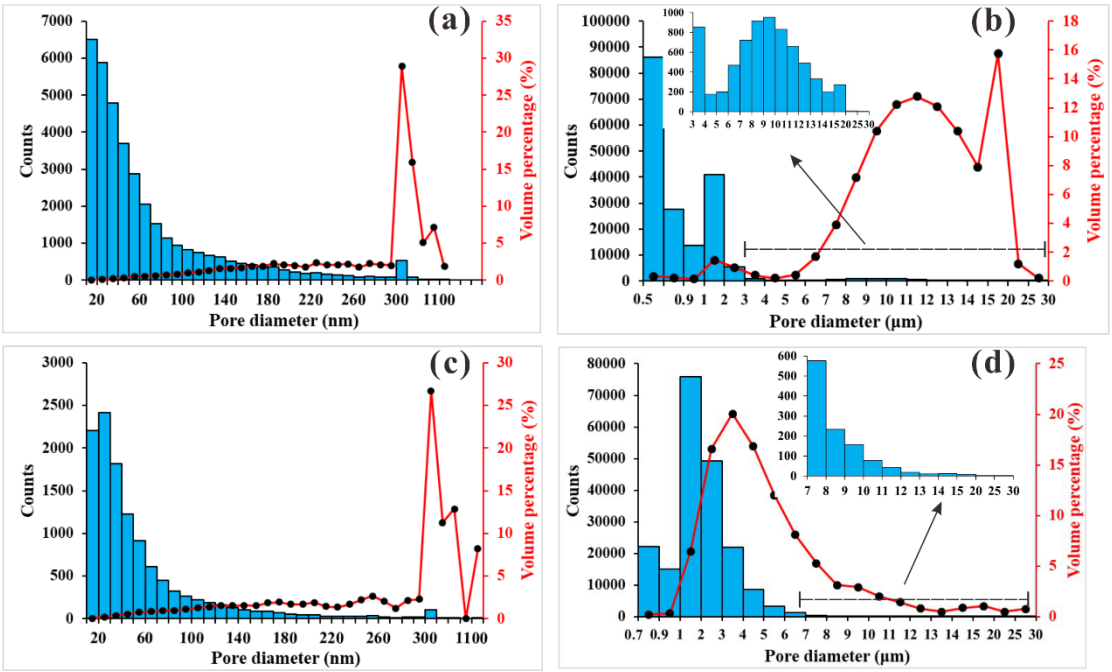

~~Fig. 5~~Fig. 6. Histogram depicting results of pore distribution and volume percentage in different ranges. (a): FIB-SEM data of sample LHG; (b): X-ray μCT data of sample LHG; (c): FIB-SEM data of sample L-1; (d): X-ray μCT data of sample L-1.

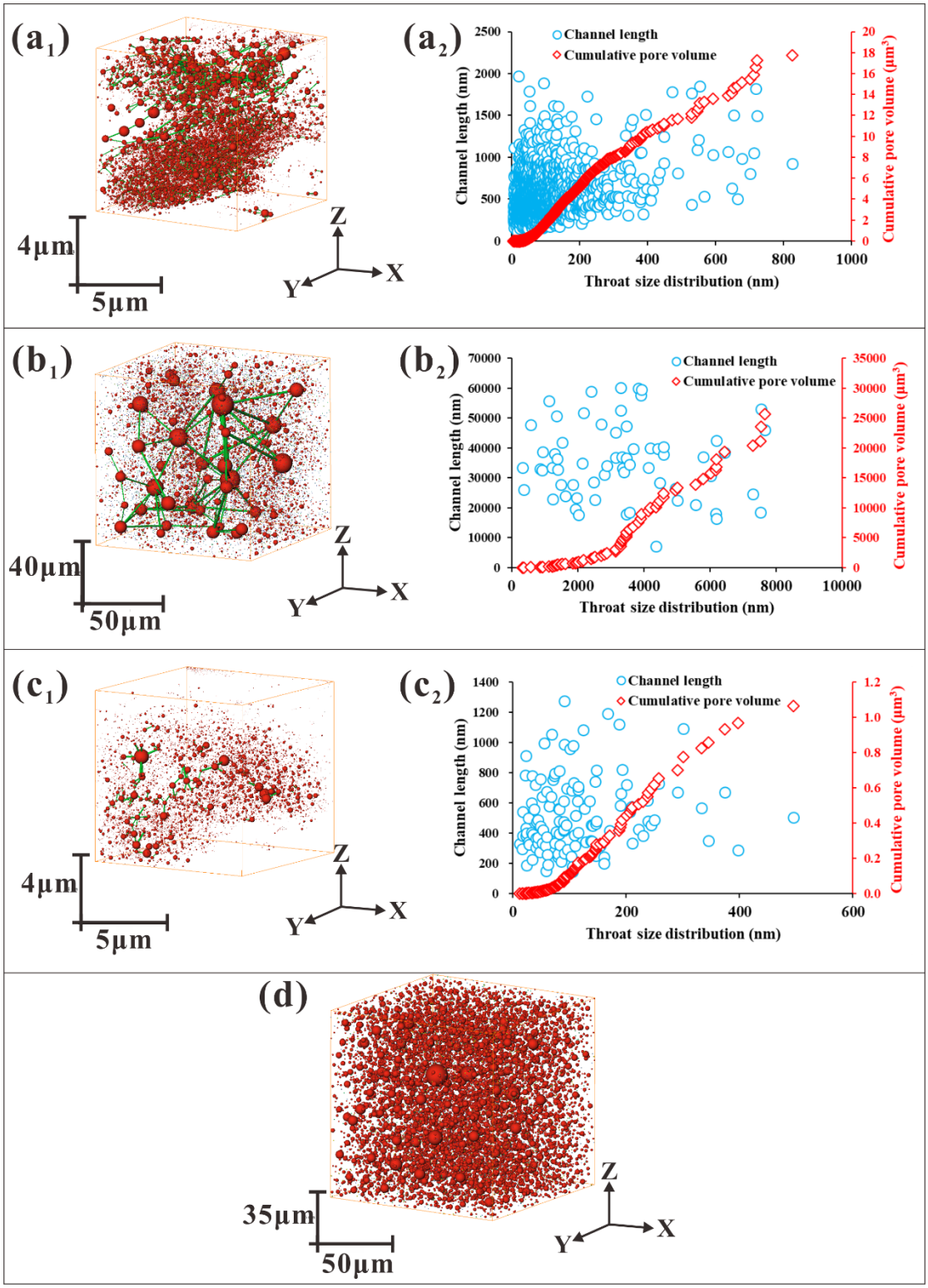

~~Fig. 6~~Fig. 7. Pore network model showing 3D pore-throat skeletal structure and distribution of throats. a_1-a_2: FIB-SEM data of sample LHG; b_1-b_2: X-ray μCT data of sample LHG; c_1-c_2: FIB-SEM data of sample L-1; d: X-ray μCT data of sample L-1.

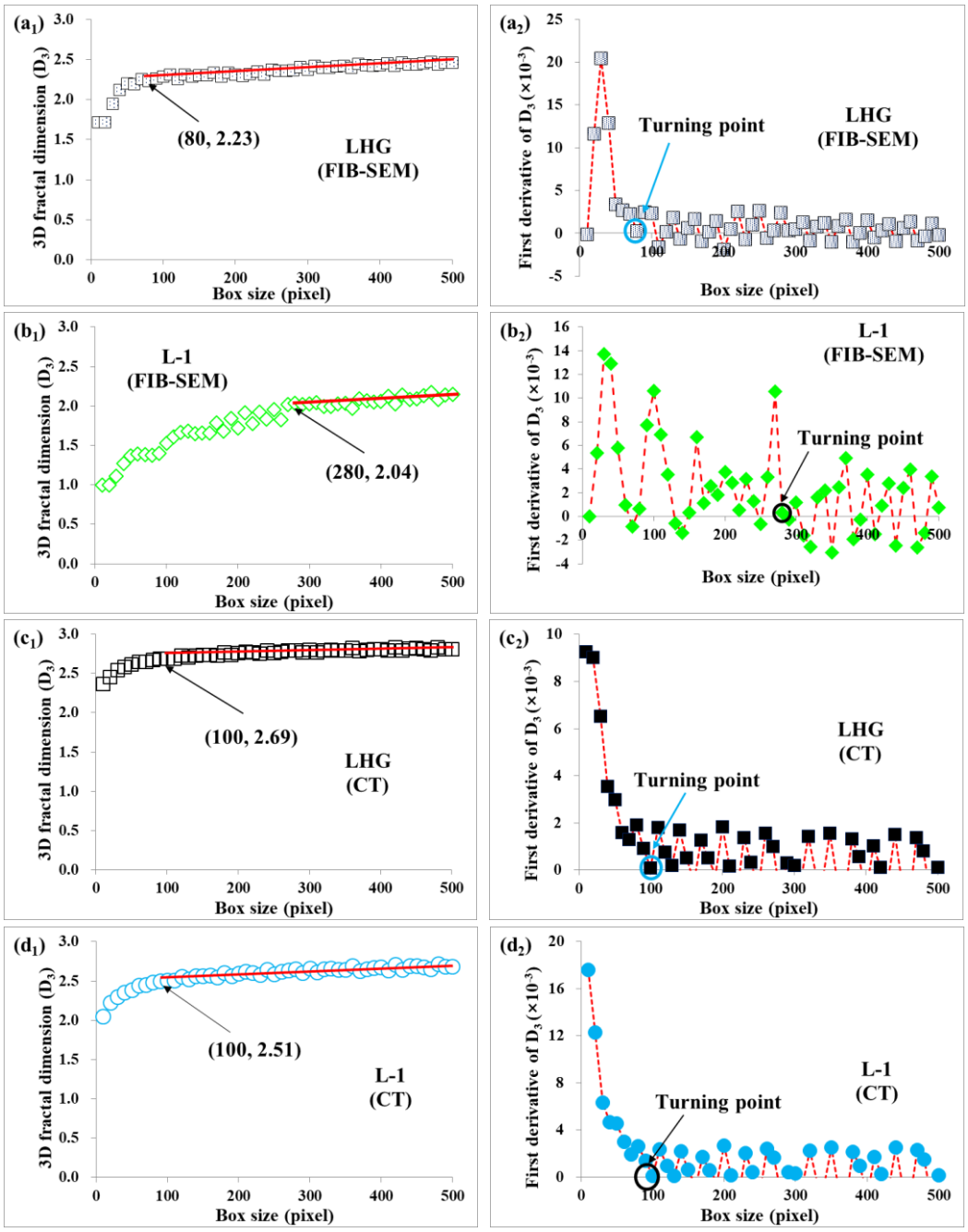

~~Fig. 7~~Fig. 8. The relationship between the three-dimensional fractal dimension (D_3) and box size. (a_1) - (d_1) is the trend of D_3 with the box size. It indicates that D_3 floats within a certain size range, but remains essentially unchanged if the calculation domain size exceeds a critical value. (a_2) - (d_2) is the first derivative of the left curve, which is used to characterize the rate of change of D_3. The point that first approaches 0 after the first derivative undergoes a significant change is defined as a turning point, which is expressed as D_3 almost stops growing from this point.

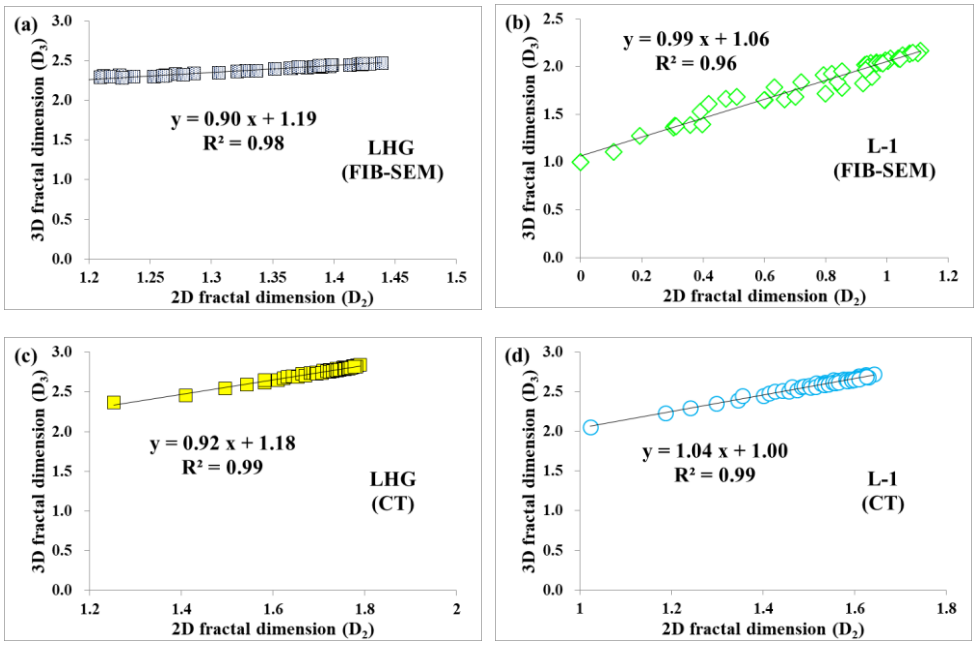

~~Fig. 8~~Fig. 9. The relationship between two-dimensional (D_2) fractal dimension and three-dimensional fractal dimension (D_3). It is found that the two-dimensional fractal dimension has a very significant linear relationship with the three-dimensional fractal dimension.

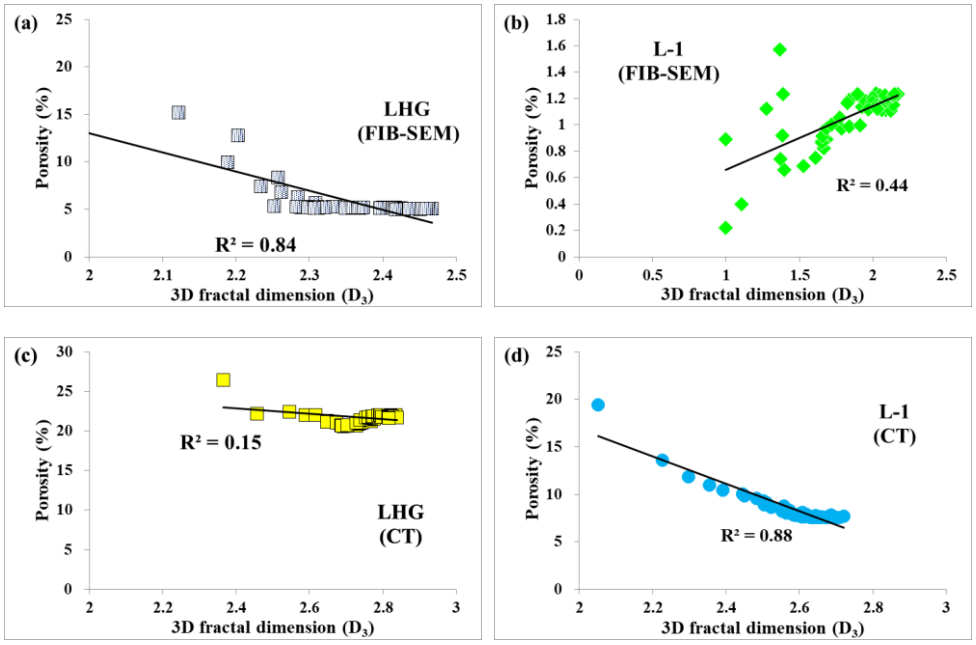

~~Fig. 9~~Fig. 10. Relationship between three-dimensional fractal dimension and porosity. (b) shows that the porosity increases with increasing D_3; that is, the porosity of sample L-1 increases as the three-dimensional spatial distribution complexity of pore-fracture system increases. (a) (c) and (d) display that the porosity decreases with the rise of D_3.

Table 1 Sample information and basic parameters of the selected Chinese coals

Sample No.	Basins	Coal Rank	$R_{o,m}$ (%)	Maceral and mineral (vol%)				Prox (wt%)			
				V	I	E	M	M_{ad}	A_{ad}	V_{ad}	FC_{ad}
LHG	Junggar	High-volatile bituminous	0.98	53.40	19.70	0.37	26.50	0.76	35.63	1.28	62.33
L-1	Qinshui	Anthracite	2.73	66.80	14.40	0.00	18.80	7.71	17.33	12.03	62.93

Note: V- Vitrinite; I - Inertinite; E- Exinite; M- Mineral; Prox- Proximate analysis; ad- as received basis; M_{ad} = moisture content; A_{ad} = ash yield; V_{ad} = volatile matter content; FC_{ad} = fixed carbon content.

Table 2 Pore size distribution characteristics of the pore-fracture system for the selected coals

Experiments	Pore diameter (nm)	Sample LHG			Sample L-1		
		Counts	Pore area (μm^2)	Pore volume (μm^3)	Counts	Pore area (μm^2)	Pore volume (μm^3)
FIB-SEM	10-100	29423	240.42	2.02	10240	89.78	0.62
	100-1000	7283	1807.86	45.37	1521	411.64	9.07
	>1000	6	57.18	4.24	1	13.92	0.87
	Total	36712	2105.45	51.63	11762	515.33	10.56
X-ray μCT	500-1000	127364	160218.62	30463.70	37177	60923.18	13292.30
	1000-10000	50802	2408362.97	1098227.32	161468	5301502.38	2151999.46
	>10000	2811	6117205.73	2986037.87	177	398234.74	189689.42
	Total	180977	8685787.31	4114728.90	198822	5760660.30	2354981.18

Table 3 Pore throat parameter information calculated by the PNM module in Avizo

Sample	Throat size (nm)	Counts	Area (μm^2)	Average channel length (μm)	Total channel length (μm)	Volume (μm^3)
LHG FIB-SEM	0-100	1188	3.23	0.52	277.70	1.69
	100-200	397	6.00	0.58	328.47	3.52
	200-300	100	4.53	0.63	228.67	2.83
	300-400	32	3.13	0.75	62.96	2.38
	400-500	9	1.37	0.88	24.12	1.25
	500-600	7	1.69	1.13	7.93	1.90
	600-700	5	1.70	0.94	4.68	1.58
	700-800	4	1.60	1.29	5.17	2.09
	800-900	1	0.54	0.92	0.92	0.50
LHG X-ray μCT	300-500	2	0.19	29.69	59.39	5.67
	500-1000	4	2.20	37.99	151.95	80.10
	1000-2000	13	23.59	33.40	434.14	732.30
	2000-3000	9	43.51	36.39	327.50	1589.28
	3000-4000	16	154.23	41.79	668.60	6541.93
	4000-5000	8	126.17	31.67	253.34	3984.68
	5000-6000	3	70.40	26.83	80.49	1929.62
	6000-7000	5	151.54	29.23	146.16	4453.54
	7000-8000	4	177.06	35.60	142.41	6352.96
L-1 FIB-SEM	10-50	29	0.03	0.46	13.30	0.01
	50-100	37	0.17	0.52	19.42	0.09
	100-200	36	0.55	0.56	20.03	0.32
	200-300	12	0.52	0.53	6.40	0.28
	300-400	5	0.49	0.59	2.96	0.27
	400-500	1	0.19	0.50	0.50	0.10

Note: X-ray μCT data of sample L-1 has no throat in the analysis.

CRediT author statement

Dameng Liu and Yidong Cai: Conceptualization and Methodology; Qian Li: Data curation, Writing- Original draft preparation; Bo Zhao: Validation; Yongkai Qiu and Yingfang Zhou: Writing- Reviewing and Editing.